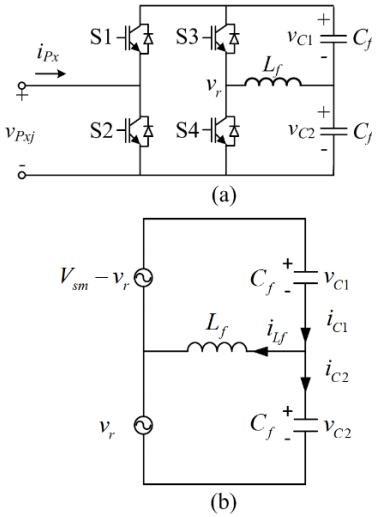

Fig. 2. (a) Topology of proposed submodule. (b) Equivalent circuit model of the power decoupling circuit.

power factor angle of the load. Note that we neglected the dc components of the powers since they don't exist in steady state.

The pulsating arm powers shown in Equ. (8) are supplied by the submodule capacitors. The lower the frequency of a power component, the larger the voltage fluctuation it will cause in the submodule capacitors. The fundamental and second-order components of the arm powers are shown in Equ. (9) and Equ. (10) (see the bottom of last page).

In a conventional submodule, the pulsating power is supplied by capacitor C_s. Since the fundamental frequency ripple power is mainly associated with the fundamental voltage fluctuation, the relationship between ripple power and fundamental frequency voltage fluctuation is

$$\frac{p_{Px\_1}}{N} = C_s \frac{dv_{1st}}{dt} V_{sm} \tag{11}$$

where V_{sm} is the dc component of the submodule voltage, v_{1st} is the instantaneous value of fundamental component in the submodule voltage. Apparently, to reduce the voltage fluctuation, the only way is to increase submodule capacitance C_s. Given the low frequencies of the ripple powers, C_s has to be very large.

In this paper, the fundamental frequency voltage fluctuation will be eliminated by the auxiliary power decoupling circuit added to each submodule. The second-order voltage fluctuation will be eliminated by proper control of circulating current. By doing so, total submodule capacitance can be significantly reduced. The following two sections deal with those two issues respectively.

III. Operating Principle, Modeling and Control of the Auxiliary Power Decoupling Circuit

The proposed submodule topology (taking the j-th one in the upper arm of phase x for example) is redrawn in Fig. 2(a), with the capacitor voltages denoted with v_{C1} and v_{C2}, for simpler subscripts. The basic idea of the power decoupling circuit is that the two split capacitors' voltages are controlled to be sinusoids with opposite phases plus dc offsets [25]. The exact voltage references for the two capacitors are such that the resulted total capacitor power (minus the inductor power) equals p_{Px_1}/N, while at the same time there will be no fundamental frequency fluctuation in the submodule voltage $v_{C1}+v_{C2}$, since the alternating parts of the two capacitor voltages always cancel out each other.

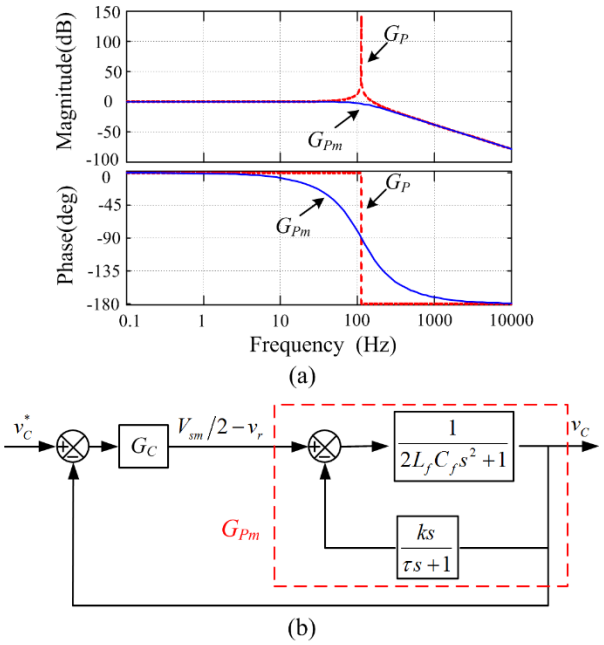

Fig. 3. (a) The effect of active damping. (b) The overall control block diagram of the power decoupling circuit.

A. Calculation of Capacitor Voltage References

Suppose the two split capacitors' voltage references to be in the form of

$$\begin{cases} v_{C1} = \frac{1}{2}V_{sm} + v_C = \frac{1}{2}V_{sm} + V_C \sin(\omega_C t + \theta_C) \\ v_{C2} = \frac{1}{2}V_{sm} - v_C = \frac{1}{2}V_{sm} - V_C \sin(\omega_C t + \theta_C) \end{cases} \tag{12}$$

where V_{sm}=v_{C1}+v_{C2} is the expected ripple-free submodule voltage (one half of which is taken here as the common dc offset), ω_C is angular frequency of the capacitor voltage, θ_C is the initial angle of the capacitor voltage, and V_C is the amplitude of the sinusoidal component.

The capacitor currents are therefore

$$\begin{cases} i_{C1} = C_f \frac{dv_{C1}}{dt} = \omega_C C_f V_C \cos(\omega_C t + \theta_C) \\ i_{C2} = C_f \frac{dv_{C2}}{dt} = -\omega_C C_f V_c \cos(\omega_C t + \theta_C) \end{cases} \tag{13}$$

With Equ. (12) and Equ. (13), total power provided by the two capacitors can be derived as

$$p_{aC} = v_{C1}i_{C1} + v_{C2}i_{C2} = \omega_C C_f V_C^2 \sin(2\omega_C t + 2\theta_C) \tag{14}$$

TABLE I
PARAMETERS OF PROPOSED MMC IN EXPERIMENTS

Items	Value
DC-link voltage: V_{dc}	500 V
Arm inductance: L	4.6 mH
No. of SMs per arm: N	2
SM voltage: V_{sm}	250 V
SM capacitance: C_f	220 μF
Filter inductance: L_f	4 mH
Switching frequency	2 kHz
Modulation index: M	0.6

According to KCL, the inductor current can be derived as

$$i_{Lf} = i_{C1} - i_{C2} \tag{15}$$

So the power of the smoothing inductor can be expressed as

$$p_{aL} = L_f \frac{di_{Lf}}{dt} i_{Lf} = -2\omega_C L_f (\omega_C C_f V_C)^2 \sin(2\omega_C t + 2\theta_C) \tag{16}$$

Hence, the total power provided by the auxiliary circuit is

$$\begin{aligned} p_a &= p_{aC} + p_{aL} \\ &= [\omega_C C_f V_C^2 - 2\omega_C L_f (\omega_C C_f V_C)^2] \sin(2\omega_C t + 2\theta_C) \end{aligned} \tag{17}$$

N times of p_a should be equal to the fundamental component of the arm power derived in Equ. (9). Since the submodule here is assumed to be one from the upper arm of phase x, this means

$$N p_a = p_{Px\_1} \tag{18}$$

With Equ. (18), V_C, ω_C and θ_C in Equ. (12) can be solved:

$$\begin{cases} \omega_C = \dfrac{1}{2}\omega \\ \theta_C = \dfrac{1}{2}\arctan\dfrac{A}{B} \\ V_C = \sqrt{\dfrac{\sqrt{A^2+B^2}}{\omega_C C_f - 2\omega_C L_f (\omega_C C_f)^2}} \end{cases} \tag{19}$$

where

$$A = \frac{1}{N}[\frac{1}{4} V_{dc} I_x \sin(\theta_x - \varphi) - V_x I_{zx\_0} \sin\theta_x - \frac{1}{2} V_x I_{zx\_2} \sin(\theta_{2x} - \theta_x)] ,$$

and

$$B = \frac{1}{N}[\frac{1}{4} V_{dc} I_x \cos(\theta_x - \varphi) - V_x I_{zx\_0} \cos\theta_x + \frac{1}{2} V_x I_{zx\_2} \sin(\theta_{2x} - \theta_x)]$$

. Note that if the submodule is from a lower arm, $\theta_C = \frac{1}{2}\arctan\frac{A}{B} + \frac{\pi}{2}$.

B. Modeling of the Power Decoupling Circuit

It is the task of the auxiliary half bridge (S3 and S4) to carry out the voltage tracking control of the two capacitors. By representing the actual (PWM style) output voltage of the half bridge with its state-space averaged value v_r, the equivalent circuit model (or the state-space averaged model) of the power decoupling circuit is shown in Fig. 2(b). v_r also serves as the modulation signal of S4, while V_{sm}-v_r is the modulation signal of S3. To properly design the tracking control system for the capacitor voltages, the relationship from v_r to the capacitor voltages (or alternating parts of them, to be precise) has to be found.

According to KVL, and neglecting the inductor's resistance, two voltage equations can be established

$$\begin{cases} v_r - V_{sm} + v_{C1} + L_f \dfrac{di_{Lf}}{dt} = 0 \\ -v_r - L_f \dfrac{di_{Lf}}{dt} + v_{C2} = 0 \end{cases} \tag{20}$$

By subtracting the two equations of Equ. (12), the sinusoidal, or the differential, component of the capacitor voltages can be found to be

$$v_C = \frac{v_{C1} - v_{C2}}{2} \tag{21}$$

With Equ. (20) and Equ. (21), the following can be obtained:

$$v_r - \frac{V_{sm}}{2} + v_C + L_f \frac{di_{Lf}}{dt} = 0 \tag{22}$$

According to Equ. (13), Equ. (15) and Equ. (21), the inductor current can be rewritten as

$$i_{Lf} = 2C_f \frac{dv_C}{dt} \tag{23}$$

Substituting Equ. (23) into Equ. (22) yields

$$2L_f C_f \frac{d^2 v_C}{dt^2} + v_C = \frac{V_{sm}}{2} - v_r \tag{24}$$

It is easy to verify that the right side of Equ. (24) is actually the alternating part of the modulation signal for S3. In light of this, it seems both convenient and useful to find the transfer function between $V_{sm}/2$-v_r and v_C, which is

$$G_P = \frac{v_C}{V_{sm}/2 - v_r} = \frac{1}{2L_f C_f s^2 + 1} \tag{25}$$

C. Control of the Power Decoupling Circuit

The controller design of the power decoupling circuit is conducted based on the parameters listed in Table I. The Bode plot of plant G_P is shown as the red dotted line in Fig. 3(a). There is a high resonance peak at the LC resonant frequency $\omega_r = 1/\sqrt{2L_f C_f}$, which is bad for system stability. In this paper, active damping by means of capacitor voltage feedback (see Fig. 3(b), which shows the overall control system) is applied to eliminate the resonance peak. Shown in Fig. 3(a) with blue solid line is the Bode plot of the modified plant G_{Pm}. The transfer function of G_{Pm} is

$$G_{Pm} = \frac{v_C}{V_{sm}/2 - v_r} = \frac{1}{2L_f C_f s^2 + \dfrac{ks}{\tau s + 1} + 1} \tag{26}$$

where k is determined by the expected damping effect, and τ is a small time constant.

A proportional plus quasi-resonant controller is adopted as the voltage controller to track the reference v_C^*, which is a 25 Hz sinusoid. Transfer function of the proportional and quasi-resonant controller is

$$G_C = K_p + \frac{2K_r\omega_b s}{s^2 + 2\omega_b s + \omega_a^2} \quad (27)$$

where ω_a = 25 Hz is the resonance frequency of the quasi-resonant controller, and ω_b is the bandwidth of the quasi-resonant controller [26].

As shown in Fig. 3(b), the output of G_C is $V_{sm}/2$-v_r. With this, modulating signals for S3 and S4 (which are V_{sm}-v_r and v_r, respectively) can be readily constructed.

D. Parameter Design of the Power Decoupling Circuit

Inductance L_f should be as small as possible, considering its weight/cost and negative contribution in supplying reactive power (see (17)). However, too small L_f may bring high switching ripple current, which raises current stress of S3 and S4. The relationship between L_f and the peak-to-peak ripple current i_{Lf_pp} is

$$i_{Lf\_pp} = \frac{V_{sm} T_s}{4L_f} \quad (28)$$

Therefore, L_f can be determined given i_{Lf_pp}.

C_f can be made smaller by applying a higher alternating component V_C across the capacitors. But V_C should not exceed its dc offset $V_{sm}/2$, i.e.

$$V_C = \sqrt{\frac{\sqrt{A^2 + B^2}}{\omega_C C_f - 2\omega_C L_f (\omega_C C_f)^2}} \le \frac{1}{2} V_{sm} \quad (29)$$

By solving Equ. (29), the constraints on C_f can be derived as

$$-C + \frac{1}{4\omega_C^2 L_f} \le C_f \le C + \frac{1}{4\omega_C^2 L_f} \quad (30)$$

where $C = \frac{\sqrt{V_{sm}^2 - 32\omega_c L_f \sqrt{A^2 + B^2}}}{4\omega_C^2 L_f V_{sm}}$. The lower limit is the one that is more useful. The reason why there is an upper limit is that too big capacitance means too high current flowing through the inductor L_f, causing the counter-productive inductor power to soar, which calls for a greater V_C (and therefore greater capacitor power to keep p_a unchanged).

IV. Elimination of Second-Order Fluctuation in Submodule Voltage

With the fundamental frequency voltage fluctuation eliminated with the auxiliary power decoupling circuit, the most significant pulsating component that remains becomes the second-order one. To eliminate the latter, a closed-loop control strategy similar to [17] is adopted, with more in-depth analysis. The basic idea is: The second-order ripple power needed by the load of the MMC has to be supplied (or balanced) by the submodule capacitors and the dc source of the MMC. The amount of contribution from the dc source is reflected by the second-order component of the circulating current i_{zx}. By proper control of the latter, the dc source can supply all the second-order ripple power while the submodules no longer supply any, hence the elimination of second-order fluctuation in the submodule voltages.

Note that there is an assumption that second-order ripple power of the submodule is solely associated with second-order ripple voltage in the submodule. It is a valid one because, even though second-order power can also be generated from fundamental frequency voltage (which has been the very idea behind the power decoupling circuit), the latter has been effectively removed from the submodule voltage by the power decoupling circuit.

The proposed control system consists of a current inner loop for tracking control of the second-order circulating current, and a voltage outer loop for suppressing the second-order fluctuation in the submodule voltage.

By taking Laplace transform of Equ. (5), the plant model of the circulating current inner loop can be derived as

$$G_{Pi} = \frac{i_{zx}}{\frac{1}{2}V_{dc} - \frac{1}{2}(v_{Px} + v_{Nx})} = \frac{i_{zx}}{v_{zx}} = \frac{1}{sL + R} \quad (31)$$

To trace the circulating current with second-order component, a proportional-integral and quasi-resonant controller is adopted with ω_a= 100 Hz. The block diagram of the circulating current control is shown in Fig. 4 (dash-line enclosed area). Each phase of the MMC needs one of such a control system.

The reference of the second-order circulating current comes from the outer loop controller, which tries to regulate the second-order component of the submodule voltage toward zero. It is known that in each phase, even-order (mainly the second order) submodule voltage fluctuations for upper and lower arms are in phase while the odd-order fluctuations are opposite in phase [28]. Therefore, total submodule voltage of each phase is roughly the summed second-order voltages plus the total dc offset $2V_{dc}$. If the $2N$ submodule voltages are well balanced, this is equivalent to say that the average submodule voltage (v_{sm}) equals the second-order voltage fluctuation (v_{2nd}) plus the dc offset V_{dc}/N in each submodule, i.e.

$$\begin{aligned} v_{sm} &= \frac{1}{2N}\left(\sum_{j=1}^{N}(v_{CPxj1} + v_{CPxj2}) + \sum_{j=1}^{N}(v_{CNxj1} + v_{CNxj2})\right) \\ &= v_{2nd} + \frac{V_{dc}}{N} \end{aligned} \quad (32)$$

To find out the plant model for the outer loop, relationship among the instantaneous powers of the dc source, the $2N$ submodules, and the load has to be investigated first. At any moment, the three powers should balance out, i.e.

$$V_{dc} i_{zx} = 2N v_{sm} C_s \frac{dv_{sm}}{dt} + p_x \quad (33)$$

where $C_s = C_f/2$ is the submodule equivalent capacitance, and p_x is the phase-x load power. Assume the first v_{sm} in Equ. (33) to be roughly V_{dc}/N for ease of analysis, and Equ. (33) can be rewritten as

$$V_{dc} i_{zx} = 2V_{dc} C_s \frac{dv_{sm}}{dt} + p_x \quad (34)$$

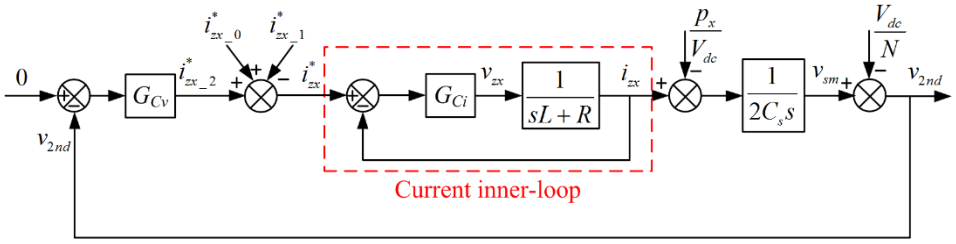

Fig. 4. Suppression control system of second-order ripple voltage.

TABLE II
PARAMETERS OF PROPOSED MMC IN SIMULATIONS

Items	Value
DC-link voltage: V_{dc}	8000 V
Rated power: P	300 kW
Arm inductance: L	1.5 mH
No. of SMs per arm: N	4
SM voltage: V_{sm}	2000 V
SM capacitance: C_f	600 μF
Filter inductance: L_f	4 mH
Switching frequency	2 kHz

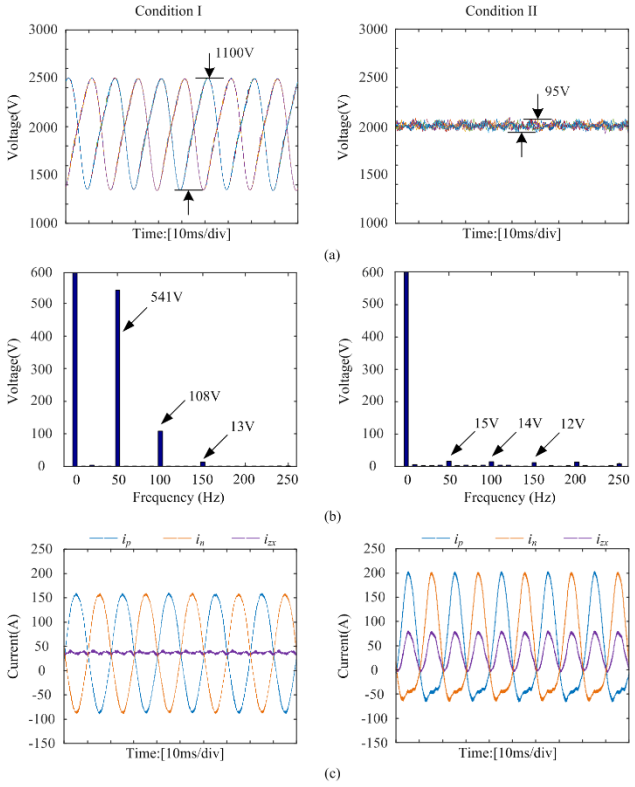

Fig. 5. Simulation waveforms of the MMC operating in Condition I & II. (a) The submodule voltages. (b) FFT analysis of one.

By taking Laplace transform of Equ. (34) and treating the load ripple power p_x as an extraneous disturbance, the transfer function from i_{zx} to v_{sm} can be obtained as

$$G_{Pv} = \frac{v_{sm}}{i_{zx}} = \frac{1}{2C_s s} \tag{35}$$

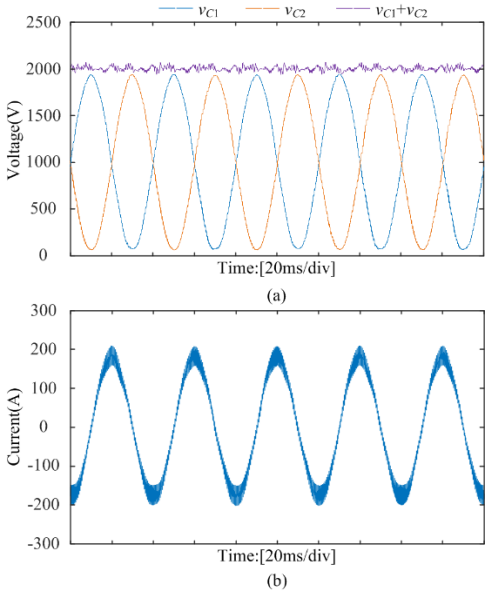

Fig. 6. Simulated voltage/current waveforms within one submodule. (a) Simulated capacitor voltages and submodule voltage. (b) Simulated current of inductor L_f (i_{Lf}).

In steady state, the power terms in Equ. (34) contain both dc and second-order components. If only second-order ripple power is concerned, Equ. (34) can be rewritten as:

$$V_{dc} i_{zx\_2} = 2V_{dc} C_s \frac{dv_{2nd}}{dt} + p_{x\_2} \tag{36}$$

where i_{zx_2} is the second-order component of i_{zx}, and p_{x_2} is the phase-x second-order ripple power of the load. The aim of the suppression control is actually to control i_{zx_2} such that the dc source provides all the second-order ripple power needed by the load, i.e. $V_{dc}\, i_{zx\_2} = p_{x\_2}$.

A proportional and quasi-resonant controller is adopted again for the outer-loop. The whole suppression control system of the second-order submodule ripple voltage is shown in Fig. 4. The reference of the second-order fluctuation is zero; and the feedback of the second-order fluctuation is provided by rewriting Equ. (32) as Equ. (37) (see the bottom of this page).

Note that the real circulating current reference i_{zx}^* has to also include its dc component $i_{zx\_0}^*$ and its fundamental component $i_{zx\_1}^*$, which come from total energy control and differential energy control [27] of the submodules, respectively. These signals are denoted in the figure but the

$$v_{2nd} = \frac{1}{2N}\left(\sum_{j=1}^{N}(v_{CPxj1} + v_{CPxj2}) + \sum_{j=1}^{N}(v_{CNxj1} + v_{CNxj2})\right) - \frac{V_{dc}}{N} = v_{sm} - \frac{V_{dc}}{N} \tag{37}$$

TABLE III
CURRENTS OF ARMS AND POWER DECOUPLING CIRCUITS

Items	Value
I_{Px_rms}	179 A
$\|I_{Px}\|_{avg}$	165 A
I_{Lf_rms}	127 A
$\|I_{Lf}\|_{avg}$	114 A

details of the related control systems are not discussed here, since (as part of converter-level control) they are not much different here.

V. SIMULATION AND EXPERIMENTAL RESULTS

A. Simulation Results

To verify the proposed method, a simulation model of a single-phase MMC inverter is established in MATLAB/Simulink. The parameters are as given in Table II. The load is a resistor.

First, to demonstrate the performance of the proposed method, two operation conditions are compared. In Condition I, the MMC is operating in conventional condition (i.e. S3 and S4 both inactive and suppression control for second-order ripple voltage turned off). In Condition II, the MMC is operating with the proposed power decoupling circuit and suppression control of second-order ripple voltage. Shown in Fig. 5 are the simulation results. It can be seen that the two most significant harmonic component, namely the fundamental and second-order ones, have been virtually eliminated with the proposed method. As a result, the peak-to-peak fluctuation of the submodule voltage is reduced from 1100 V to 95 V. For a conventional submodule (as shown in Fig. 1(b)) to obtain the same suppression effect, a 3.5 mF capacitance would be required.

With the suppression control of second-order ripple voltage, second-order ripple power is transferred from the submodules to the dc source. Therefore, there is a second-order component in circulating current, and both arm currents are shifted upward a bit.

Fig. 6(a) and (b) shows the capacitor voltages, the submodule voltage, and inductor current within one submodule of the modified MMC in simulations. The ripple current can be further reduced if higher switching frequency is adopted. The fundamental component of the inductor current is roughly the same as the arm current, indicating a same level of current stresses for S1/S2 and S3/S4.

B. Power Loss Comparison

Introducing active circuitry into the submodule will inevitably affect the efficiency. To assess the effect, the power losses associated with IGBTs and diodes of conventional MMC and the proposed MMC are compared. The loss calculation method in reference [29] is adopted.

IGBT and diode power losses can be classified into conduction losses, switching losses and blocking losses (usually neglected). When calculating conduction losses, the simplified model of IGBT with a voltage source (v_{CE0}) representing on-state zero-current collector-emitter voltage and a series-connected collector-emitter on-state resistance (r_C) is used. Similarly, the same approximation can be used for the anti-parallel diode. Hence, instantaneous value of conduction loss for the IGBT (p_{CT}) and the diode (p_{CD}) can be expressed as:

$$\begin{cases} p_{CT} = v_{CE0} i_C + r_C i_C^2 \\ p_{CD} = v_{D0} i_D + r_D i_D^2 \end{cases} \tag{38}$$

Take the half-bridge S1/S2 in Fig.1 (c) for example. When $i_{Px} > 0$, the average conduction loss in one fundamental period ($1/f_1$) is:

$$\begin{aligned} P_{C1} = {} & f_1 \int_t^{t+1/f_1} \left(v_{D0} i_{Px} + r_D i_{Px}^2 \right) S(\tau) d\tau \\ & + f_1 \int_t^{t+1/f_1} \left(v_{CE0} i_{Px} + r_C i_{Px}^2 \right) \left[1 - S(\tau) \right] d\tau \end{aligned} \tag{39}$$

where $S(t)$ is the switching function and is defined as:
$S(t) = 1$: S1 on and S2 off, SM capacitor inserted;
$S(t) = 0$: S1 off and S2 on, SM capacitor bypassed.

Similarly, when $i_{Px} < 0$, the average conduction loss is:

$$\begin{aligned} P_{C2} = {} & f_1 \int_t^{t+1/f_1} \left[v_{CE0} \left(-i_{Px} \right) + r_C i_{Px}^2 \right] S(\tau) d\tau \\ & + f_1 \int_t^{t+1/f_1} \left[v_{D0} \left(-i_{Px} \right) + r_D i_{Px}^2 \right] \left[1 - S(\tau) \right] d\tau \end{aligned} \tag{40}$$

Assume the time interval in which $i_{Px} > 0$ to be T_P, and combine Equ. (39) and Equ. (40), then the average conduction loss in one fundamental period ($1/f_1$) can be derived as

$$\begin{aligned} P_C &= \frac{T_P}{1/f_1} P_{C1} + \left(1 - \frac{T_P}{1/f_1} \right) P_{C2} \\ &= \frac{T_P}{1/f_1} \left(v_{CE0} \left| I_{Px} \right|_{avg} + r_C I_{Px\_rms}^2 \right) + \left(1 - \frac{T_P}{1/f_1} \right) \left(v_{D0} \left| I_{Px} \right|_{avg} + r_D I_{Px\_rms}^2 \right) \end{aligned} \tag{41}$$

where $|I_{Px}|_{avg}$ is the average value of absolute arm current, I_{Px_rms} is the root-mean-square value of arm current.

Based on specific curves depicting the various switching energy losses against the current, which can be found from power device datasheets, switching loss (P_{sw}) is approximated as:

$$P_{sw} = f_s \left(E_{onT} + E_{offT} + E_{rec} \right) \tag{42}$$

where E_{onT} and E_{offT} are the switch-on and switch-off energy losses of IGBT, E_{rec} is the reverse-recovery energy loss of diode.

In the simulation model, Infineon FD400R33KL2C IGBT module is chosen. The parameters for power loss calculation can be read from the IGBT datasheet [30]. The currents of arms and power decoupling circuits are listed in Table III. According to Equ. (41) and Equ. (42), the power losses of the conventional MMC and the proposed MMC can be estimated. It is found that the efficiency of the conventional MMC is

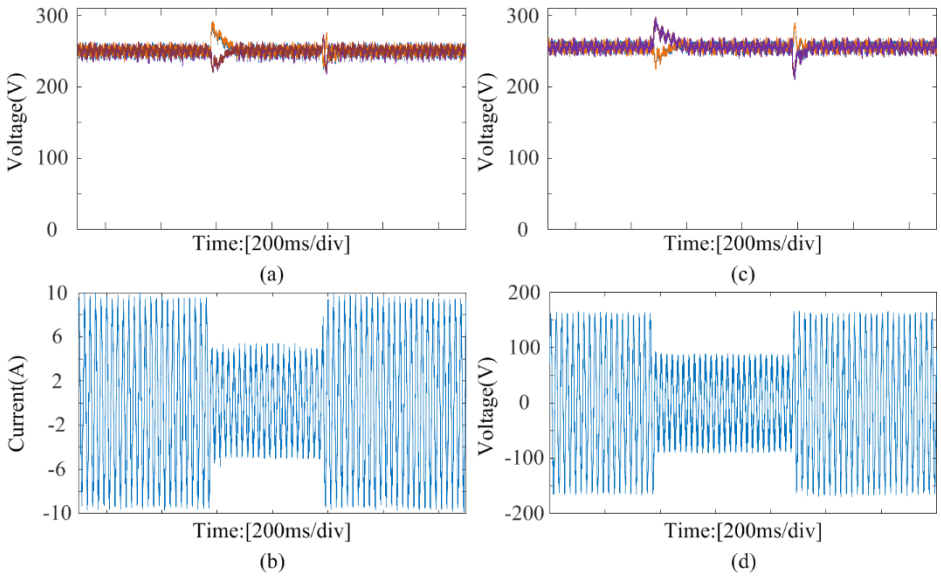

Fig. 9. Experimental waveforms during transient processes. (a) Submodule voltages with 50% step-down and step-up of load current. (b) Output current with 50% step-down and step-up of load current. (c) Submodule voltages with 50% step-down and step-up of modulation index. (d) Output voltage with 50% step-down and step-up of modulation index.

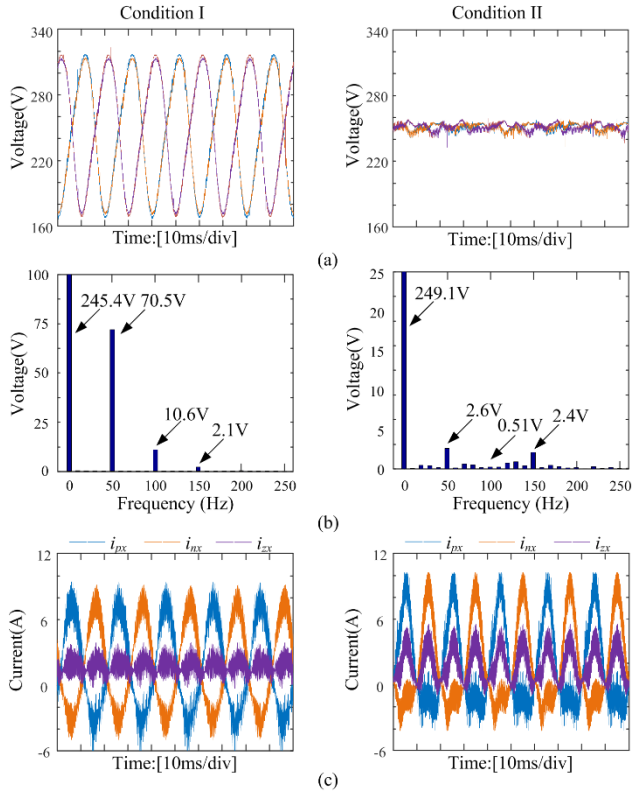

Fig. 7. Experimental waveforms of the MMC operating in Condition I & II. (a) The submodule voltages. (b) FFT analysis of one submodule voltage. (c) The arm currents and circulating current.

97.91%, and the efficiency of the proposed MMC is 96.06%. The decrease in efficiency is mild considering the significant reduction of submodule capacitance.

C. *Experimental Results*

Experiments were made on a single-phase MMC test setup.

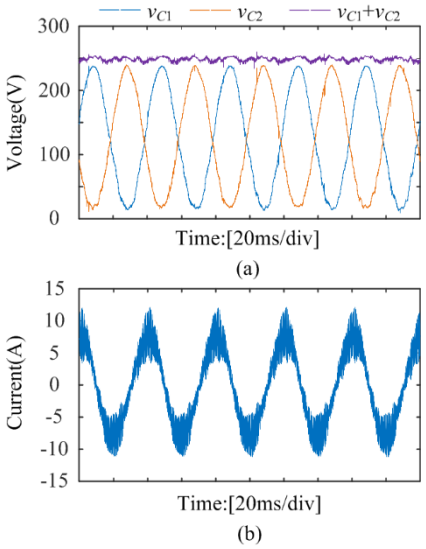

Fig. 8. Experimental voltage/current waveforms within one submodule. (a) Experimental capacitor voltages and submodule voltage. (b) Experimental current of inductor L_f (i_{Lf}).

The parameters are as listed in Table I. The load is a resistor. The control system is implemented with a TMS320F2812 DSP from Texas Instruments. An EP1C12Q240I7 FPGA performs the pulse-width modulation.

Experimental comparisons of submodule voltages, arm currents and circulating currents with Condition I and II (as described in Section 5-A) are presented in Fig. 7. Similar to the simulation results in Fig. 5, the fundamental and second-order fluctuation voltages are effectively suppressed, with the peak-to-peak fluctuation of the submodule voltage reduced from 148 V to 18 V.

Fig. 8(a) and (b) shows the capacitor voltages, the submodule voltage, and inductor current within one submodule of the modified MMC in experiments. The results

are similar to the simulation results presented in Fig. 6(a) and (b).

Experimental waveforms during transient processes are presented in Fig. 9. Two kinds of transients are investigated: load step changes and step changes of modulation index (which determines the output voltage). As shown in Fig. 9, the submodule voltage dips/swells during transients are well within 20% of the rated voltage. There are no visible low-frequency fluctuations in the submodule voltages during the transients. And the submodule voltages can converge to their rated values within 5 line cycles.

VI. CONCLUSIONS

The submodule capacitors in an MMC are usually quite bulky since they have to withstand fundamental-frequency and second-order voltage fluctuations. The capacitors therefore constitute a major part in the cost and volume of an MMC. In this paper, a power decoupling circuit is added to the conventional submodule topology, so that the fundamental frequency voltage fluctuation is eliminated at the submodule level. A circulating current-based closed-loop control system is then employed to eliminate the remaining second-order fluctuation. Simulations and experiments prove that the proposed method works well, and the two major submodule voltage fluctuation components are suppressed effectively. The submodule capacitance can be reduced roughly three-fold. Although the modified submodule uses two more active devices and a smoothing inductor, the total volume and cost of the MMC system may still be reduced, especially when considering the fact that new generations of power devices (and their driving circuits) always come out with higher performance and lower cost (and even smaller sizes). The smoothing inductor can also be reduced with higher switching frequencies. This paper provides a candidate solution for MV application where power density is given a high priority.

ACKNOWLEDGMENT

This work was supported by the National Natural Science Foundation of China (Project No.51477063).

REFERENCES

[1] H. Liu, K. Ma, Z. Qin, P. C. Loh and F. Blaabjerg, "Lifetime Estimation of MMC for Offshore Wind Power HVDC Application," *IEEE J. Emerg. Sel. Topics Power Electron.*, Vol. 4, No. 2, pp. 504-511, Jun. 2016.

[2] Y. Chen, Z. Li, S. Zhao, X. Wei and Y. Kang, "Design and Implementation of A Modular Multilevel Converter (MMC) wtih Hierarchical Redundancy Ability for Electric Ship MVDC System," *IEEE J. Emerg. Sel. Topics Power Electron.*, Vol. 5, No. 1, pp. 189-202, Mar. 2017.

[3] S. Du and J. Liu, "A Study on DC Voltage Control for Chopper-Cell-Based Modular Multilevel Converters in D-STATCOM Application," *IEEE Trans. Power Del.*, Vol. 28, No. 4, pp. 2030-2038, Oct. 2013.

[4] Z. Shu, M. Liu, L. Zhao, S. Song, Q. Zhou and X. He, "Predictive Harmonic Control and Its Optimal Digital Implementation for MMC-Based Active Power Filter," *IEEE Trans. Ind. Electron.*, Vol. 63, No. 8, pp.Aug. 2016.

[5] S. Kouro, M. Malinowski, K. Gopakumar, J. Pou, L. G. Franquelo, B. Wu, J. Rodriguez, M. A. Perez and J. I. Leon, "Recent Advances and Industrial Applications of Multilevel Converters," *IEEE Trans. Ind. Electron.*, Vol. 57, No. 8, pp. 2553-2580, Aug. 2010.

[6] A. Lesnicar and R. Marquardt, "An Innovative Modular Multilevel Converter Topology Suitable for a Wide Power Range," *in Proc. Power Tech Conference*, pp. 6, 2003.

[7] A. Alexander and M. Thathan, "Cell capacitor sizing in multilevel converters: cases of the modular multilevel converter and alternate arm converter," *IET Renewable Power Generation*, Vol. 9, No. 1, pp. 78-88, Mar. 2015.

[8] A. J. Korn, D. M. Winkelnkemper and D. P. Steimer, "Low Output Frequency Operation of the Modular Multi-Level Converter," *in Proc. IEEE Energy Convers. Congr. Expo.*, pp. 3993-3997, 2010.

[9] K. Ilves, A. Antonopoulos, L. Harnefors, S. Norrga, L. Angquist and H. Nee, "Capacitor Voltage Ripple Shaping in Modular Multilevel Converters Allowing for Operating Region Extension," *in Proc. Industrial Electronics, Control and Instrumentation*, pp. 4403-4408, 2011.

[10] S. Debnath and M. Saeedifard, "Optimal Control of Modular Multilevel Converters for Low-Speed Operation of Motor Drives," *in Proc. IEEE Applied Power Electronics Conf.*, pp. 247-254, 2014.

[11] J. Jung, H. Lee and S. Sul, "Control Strategy for Improved Dynamic Performance of Variable-Speed Drives With Modular Multilevel Converter," *IEEE J. Emerg. Sel. Topics Power Electron.*, Vol. 3, No. 2, pp. 371-380, Jun. 2015.

[12] A. Antonopoulos, L. Angquist, S. Norrga, K. Ilves, L. Harnefors and H. Nee, "Modular Multilevel Converter AC Motor Drives With Constant Torque From Zero to Nominal Speed," *IEEE Trans. Ind. Appl.*, Vol. 50, No. 3, pp. 1982-1993, May/Jun. 2014.

[13] J. Kolb, F. Kammerer, M. Gommeringer and M. Braun, "Cascaded Control System of the Modular Multilevel Converter for Feeding Variable-Speed Drives," *IEEE Trans. Power Electron.*, Vol. 30, No. 1, pp. 349-357, Jan. 2015.

[14] M. Hagiwara, I. Hasegawa and H. Akagi, "Start-Up and Low-Speed Operation of an Electric Motor Driven by a Modular Multilevel Cascade Inverter," *IEEE Trans. Ind. Appl.*, Vol. 49, No. 4, pp. 1556-1565, Jul./Aug. 2013.

[15] K. Wang, Y. Li, Z. Zheng and L. Xu, "Voltage Balancing and Fluctuation-Suppression Methods of Floating Capacitors in a New Modular Multilevel Converter," *IEEE Trans. Ind. Electron.*, Vol. 60, No. 5, pp. 1943-1954, May 2013.

[16] L. He, K. Zhang, J. Xiong, S. Fan, X. Chen and Y. Xue, "New Modular Multilevel Converter with Power Channels between Upper- and Lower Arms Suitable for MV Drives," *in Proc. IEEE Applied Power Electronics Conf.*, pp. 799-805, 2015.

[17] B. Li, Y. Zhang, G. Wang, W. Sun, D. Xu and W. Wang, "A Modified Modular Multilevel Converter With Reduced Capacitor Voltage Fluctuation," *IEEE Trans. Ind. Electron.*, Vol. 62, No. 10, pp. 6108-6119, Oct. 2015.

[18] T. Shimizu, Y. Jin and G. Kimura, "DC Ripple Current Reduction on a Single-Phase PWM Voltage-Source Rectifier," *IEEE Trans. Ind. Appl.*, Vol. 36, No. 5, pp. 1419-1429, Sept./Oct. 2000.

[19] K. Tsuno, T. Shimizu, K. Wada and K. Ishii, "Optimization of the DC Ripple Energy Compensating Circuit," *in Proc. Power Electronics Specialists Conference*, pp. 316-321, 2004.

[20] K. Chao, P. Cheng and T. Shimizu, "New Control Methods for Single Phase PWM Regenerative Rectifier with Power Decoupling Function," *in Proc. Power Electronics and Drive Systems*, pp. 1091-1096, 2009.

[21] R. Wang, F. Wang, D. Boroyevich, R. Burgos, R. Lai, P. Ning and K. Rajashekara, "A High Power Density Single-Phase PWM Rectifier With Active Ripple Energy Storage," *IEEE Trans. Power Electron.*, Vol. 26, No. 5, pp. 1430-1443, May 2011.

[22] H. Li, K. Zhang, H. Zhao, S. Fan and J. Xiong, "Active Power Decoupling for High-Power Single-Phase PWM Rectifiers," *IEEE Trans. Power Electron.*, Vol. 28, No. 3, pp. 1308-1319, Mar. 2013.

[23] W. Qi, H. Wang, X. Tan, G. Wang and K. D. T. Ngo, "A novel active power decoupling single-phase PWM rectifier topology," *in Proc. IEEE Applied Power Electronics Conf.*, pp. 89-95, 2014.

[24] Y. Tang, F. Blaabjerg, P. C. Loh, C. Jin and P. Wang, "Decoupling of Fluctuating Power in Single-Phase Systems Through a Symmetrical Half-Bridge Circuit," *IEEE Trans. Power Electron.*, Vol. 30, No. 4, pp. 1855-1865, Apr. 2015.

[25] H. Zhao, H. Li, C. Min and K. Zhang, "A modified single-phase h-bridge PWM rectifier with power decoupling," *in Proc. Industrial Electronics, Control and Instrumentation*, pp. 80-85, 2012.

[26] D. N. Zmood and D. G. Holmes, "Stationary frame current regulation of PWM inverters with zero steady-state error," *IEEE Trans. Power Electron.*, Vol. 18, No. 3, pp. 814-822, May 2003.

[27] S. Fan, K. Zhang, J. Xiong and Y. Xue, "An Improved Control System for Modular Multilevel Converters with New Modulation Strategy and Voltage Balancing Control," *IEEE Trans. Power Electron.*, Vol. 30, No. 1, pp. 358-371, Jan. 2015.

[28] Q. Song, W. Liu, X. Li, H. Rao, S. Xu and L. Li, "A Steady-State Analysis Method for a Modular Multilevel Converter," *IEEE Trans. Power Electron.*, Vol. 28, No. 8, pp. 3702-3713, Aug. 2013.

[29] D. Graovac and M. Pürschel, "IGBT power losses calculation using the datasheet parameters," Infineon Technol., Neubiberg, Germany, Appl. Note, vol. 1, Jan. 2009, pp. 1–17.

[30] Infineon FD400R33KL2C, [Online]. Available: http://www.infineon.com.

Xin Huang was born in Jiangsu, China, in 1989. He received the B.E. degree from the Huazhong University of Science and Technology (HUST), Wuhan, China, in 2012. He is currently working toward the Ph.D. degree at the School of Electrical and Electronics Engineering, Huazhong University of Science and Technology (HUST), Wuhan, China. His research interests include design and control of power electronics systems, ac drives, and modular multilevel converters.

Kai Zhang received his B.S., M.S. and Ph.D. degrees from the Huazhong University of Science and Technology (HUST), Wuhan, China, in 1993, 1996 and 2001, respectively. He joined HUST as an Assistant Lecturer in 1996, and was promoted to Full Professor in 2006. He was a Visiting Scholar at the University of New Brunswick, Fredericton, NB, Canada, from 2004 to 2005. He is the author of more than 60 technical papers. His current research interests include uninterruptible power systems, railway traction drives, modular multilevel converters, and electromagnetic compatibility techniques for power electronic systems.

Jingbo Kan was born in Shandong Province, China. He received the B.E. degree from the Shandong University, Jinan, China, in 2004, and the M.E. degree from Anhui University of Technology, Maanshan, China, in 2009. He is currently working toward the Ph.D. degree at the School of Electrical and Electronics Engineering, Huazhong University of Science and Technology (HUST), Wuhan, China. His research interests include railway traction drives and optimized pulsewidth modulation techniques.

Jian Xiong received his B.S. degree from the East China Shipbuilding Institute, Zhenjiang, China, in 1993; and his M.S. and Ph.D. degrees from the Huazhong University of Science and Technology (HUST), Wuhan, China, in 1996 and 1999, respectively. He joined HUST as a Lecturer in 1999, and became an Associate Professor in 2003. His current research interests include uninterruptible power systems, ac drives, switch-mode rectifiers, STATCOMs, and their related control techniques.